

# A 20-Gbps Beam-Steered Infrared Wireless Link Enabled by a Passively Field-Programmable Metasurface

**Citation for published version (APA):**

Huang, J., Li, C., Lei, Y., Yang, L., Xiang, Y., Curto, A. G., Li, Z., Guo, L., Cao, Z., Hao, Y., & Koonen, A. M. J. (2021). A 20-Gbps Beam-Steered Infrared Wireless Link Enabled by a Passively Field-Programmable Metasurface. *Laser & Photonics reviews*, 15(1), Article 2000266. Advance online publication. <https://doi.org/10.1002/lpor.202000266>

**DOI:**

[10.1002/lpor.202000266](https://doi.org/10.1002/lpor.202000266)

**Document status and date:**

Published: 01/01/2021

**Document Version:**

Publisher's PDF, also known as Version of Record (includes final page, issue and volume numbers)

**Please check the document version of this publication:**

- A submitted manuscript is the version of the article upon submission and before peer-review. There can be important differences between the submitted version and the official published version of record. People interested in the research are advised to contact the author for the final version of the publication, or visit the DOI to the publisher's website.
- The final author version and the galley proof are versions of the publication after peer review.
- The final published version features the final layout of the paper including the volume, issue and page numbers.

[Link to publication](#)

**General rights**

Copyright and moral rights for the publications made accessible in the public portal are retained by the authors and/or other copyright owners and it is a condition of accessing publications that users recognise and abide by the legal requirements associated with these rights.

- Users may download and print one copy of any publication from the public portal for the purpose of private study or research.
- You may not further distribute the material or use it for any profit-making activity or commercial gain
- You may freely distribute the URL identifying the publication in the public portal.

If the publication is distributed under the terms of Article 25fa of the Dutch Copyright Act, indicated by the "Taverne" license above, please follow below link for the End User Agreement:

[www.tue.nl/taverne](http://www.tue.nl/taverne)

**Take down policy**

If you believe that this document breaches copyright please contact us at:

[openaccess@tue.nl](mailto:openaccess@tue.nl)

providing details and we will investigate your claim.

# A 20-Gbps Beam-Steered Infrared Wireless Link Enabled by a Passively Field-Programmable Metasurface

Jianou Huang, Chao Li, Yu Lei, Ling Yang, Yuanjiang Xiang, Alberto G. Curto, Zilun Li, Lei Guo,\* Zizheng Cao,\* Yue Hao, and Antonius Marcellus Jozef Koonen

**Beam steering is one of the main challenges in energy-efficient and high-speed infrared light communication. To date, active beam-steering schemes based on a spatial light modulator (SLM) or micro-electrical mechanical system (MEMS) mirror, as well as the passive ones based on diffractive gratings, are demonstrated for infrared light communication. Here, for the first time to the authors' knowledge, an infrared beam is steered by 35° on one side empowered by a passively field-programmable metasurface. By combining the centralized control of wavelength and polarization, a remote passive metasurface can steer the infrared beam in a remote access point. The proposed system has the scalability to support multiple beams, flexibility to steer the beam, high optical efficiency, simple and cheap devices on remote sides, and centralized control (low maintenance cost), while it avoids disadvantages such as grating loss, a small coverage area, and a bulky size. Based on the proposed beam-steering technology, a proof-of-concept experiment system with a data rate of 20 Gbps is also demonstrated.**

## 1. Introduction

With the explosive growth of the number of broadband mobile devices and the rapid development of the Internet of Things,<sup>[1]</sup> the booming demand for high-speed wireless connectivity is challenging the existing radio wireless communication solutions, especially in indoor scenarios. The widely used wireless technology Wi-Fi suffers from a limited data rate because the data are modulated on a narrow band and transmitted at low carrier frequencies such as 2.4 GHz and 5 GHz. More importantly, this capacity is shared among multiple users. The latest IEEE 802.11ac standard provides a channel bandwidth of up to 160 MHz in the 5 GHz spectrum, with a physical-layer data rate of up to 6.93 Gbps.<sup>[2]</sup> Nevertheless, the

radio spectrum is still overwhelmed by the ever-increasing high-speed connection demands.

As an alternative, optical wireless communication (OWC) has recently attracted much interest because it can provide a high wireless connection capacity in an indoor environment. Hence, OWC can largely solve the shortage of radio spectrum resources.<sup>[3]</sup> Visible light communication (VLC)<sup>[4]</sup> and beam-steered infrared (IR) light communication (BS-ILC)<sup>[5,6]</sup> are the two main technical directions of OWC. VLC transports data over LED illumination systems and multiple users share the VLC capacity. It provides access to a bandwidth of no less than 320 THz in the 400–700 nm range.<sup>[3]</sup> BS-ILC uses well-directed narrow IR beams to establish point-to-point communication channels. Multiple users are served by a corresponding number of IR beams. Each user has an independent connection to the transmitter, which guarantees capacity and data safety. Furthermore, directed narrow IR beams can provide high energy efficiency. Moreover, because a relatively high transmitted power of IR light is allowed in terms of eye safety, BS-ILC can achieve a very high data rate and system capacity. For VLC and BS-ILC, capacities >10 Gbps<sup>[7]</sup> and >400 Gbps<sup>[8]</sup> have been demonstrated in the laboratory, respectively.

However, as a prerequisite for BS-ILC, the 2D IR beam steering approach is still the main challenge toward the practical realization of BS-ILC. Spatial light modulator (SLM)-based<sup>[9,10]</sup> and micro-electrical mechanical system (MEMS)-mirror-based<sup>[11]</sup> active beam steering solutions have been proposed. When


J. Huang, Dr. C. Li, Y. Lei, Dr. A. G. Curto, Dr. Z. Cao, Prof. A. M. J. Koonen  
Eindhoven University of Technology  
Eindhoven 5600MB, The Netherlands  
E-mail: z.cao@tue.nl

Dr. L. Yang, Prof. Y. Hao  
State Key Discipline Laboratory of Wide Band-Gap Semiconductor  
Technology  
Xidian University  
Xi'an 710071, China

Dr. Z. Li  
Division of Vascular Surgery  
The First Affiliated Hospital of Sun Yat-sen University  
Guangzhou 510080, China

Prof. Y. Xiang  
School of Physics and Electronics  
Hunan University  
Changsha 410082, China

Prof. L. Guo  
School of Communication and Information Engineering  
Chongqing University of Posts and Telecommunications  
Chongqing 400065, China  
E-mail: guolei@cqupt.edu.cn

 The ORCID identification number(s) for the author(s) of this article can be found under <https://doi.org/10.1002/lpor.202000266>

© 2020 The Authors. Published by Wiley-VCH GmbH. This is an open access article under the terms of the Creative Commons Attribution License, which permits use, distribution and reproduction in any medium, provided the original work is properly cited.

DOI: 10.1002/lpor.202000266

using MEMS-based mirrors, a large beam steering angle can be achieved by mechanically tuning the small mirrors, but it is difficult to realize multi-beam operation because multiple steering elements are needed, resulting in complex control schemes and system configurations. For SLM-based approaches, the IR beam can be steered by electronically tuning the phase with the SLM. No mechanical movement is introduced. Hence, quick and stable steering is realized. However, SLM-based systems are relatively bulky because complicated angle magnifiers are needed as the SLM itself can only provide very limited steering angle ( $\approx 3^\circ$ ). Additionally, grating loss is introduced, and the scalability toward many beams is limited.

Passive beam-steering solutions<sup>[12–17]</sup> are therefore more accessible. The beam directions are mapped to the wavelengths. By inputting many wavelengths to the system through a fiber, the corresponding beam directions can be enabled simultaneously. Gratings,<sup>[12,13]</sup> phased arrays,<sup>[14]</sup> grating couplers,<sup>[15]</sup> and arrayed waveguide grating routers (AWGRs)<sup>[16,17]</sup> have been applied to realize fully passive 2D IR beam-steering systems. Among them, AWGR-based beam-steering modules<sup>[16,17]</sup> have obvious advantages: a 2D angular range of  $17^\circ \times 17^\circ$ , compact size, high efficiency, full area coverage, fast steering speed, 80 independent beams, and a data rate per beam of 112 Gbps, which indicate a huge system capacity of 8.96 Tbps.

Here, we present a novel solution to IR beam steering based on a passively field-programmable metasurface. Metasurfaces are an emerging approach to manipulate electromagnetic (EM) waves. They are generally created by assembling arrays of sub-wavelength resonators to provide full control of the phase, amplitude, and polarization of EM waves.<sup>[18–20]</sup> Hence, actively tunable metasurfaces are widely considered for realizing beam steering.<sup>[21–25]</sup> Tunable metasurfaces can be dynamically controlled via external stimuli, which are usually electrical biases, laser pulses, or heat inputs. Owing to the sub-wavelength scale of the resonators, controlling every resonator is difficult and would make the structure very complicated and difficult to manufacture, particularly in the optical range. Therefore, tunable metasurface-based beam steering is usually realized at microwave frequencies.<sup>[24,25]</sup> In the optical range, controlling every resonator is unrealistic, yielding very limited beam steering.<sup>[23]</sup> On the other hand, beam steering based on a passive metasurface is proposed by Ding et al.<sup>[26]</sup> Similar to the approach using grating, wavelength tuning is applied to change the beam direction. However, only the +1 diffraction order can be used in the metasurface while the other diffraction orders are strongly suppressed. Although high efficiency can be obtained, the steering angle is limited and a very wide wavelength tuning range is needed ( $7.3^\circ$  steering angle is achieved over a wide spectral range of 580–700 nm in ref. [26]).

In our system, a polarization beam splitter based on a passive gap-surface plasmon metasurface (GSPM) is applied for 2D IR beam steering. GSPM has the advantages of high efficiency, excellent control over the reflected or transmitted light, and a simple manufacturing technique.<sup>[27]</sup> It has been used to realize numerous flat devices such as anomalous reflectors,<sup>[28]</sup> focusing flat mirrors,<sup>[29]</sup> phase modulators,<sup>[30]</sup> holograms,<sup>[31]</sup> polarisation beam splitters,<sup>[32]</sup> metagratings,<sup>[33]</sup> and orbital angular momentum generators.<sup>[34–36]</sup> With the GSPM-based beam splitter and a simple liquid-crystal polarization controller, polarization-

controlled beam steering can be realized. Together with an AWGR-based beam-steering module, a polarization-wavelength-controlled 2D IR beam-steering system is achieved. The new system keeps all the advantages of AWGR-based beam-steering approaches,<sup>[16,17]</sup> and additionally has polarization control capability. Hence, the coverage is greatly expanded. Furthermore, the grating loss existing in SLM-based and grating-based beam-steering approaches can be avoided by using the metasurface, which improves the energy efficiency. Finally, a metasurface polarization beam splitter is designed, fabricated, and measured. With the metasurface chip, polarization-controlled 2D IR beam steering experiments are performed in a broad wavelength band, and a 20-Gbps beam-steered infrared wireless link is built over 1.2-m free space, which proves the feasibility of the proposed 2D IR beam steering system.

## 2. Architecture and Operation Principle

The proposed 2D IR beam-steering system is shown in **Figure 1**. It is composed of an AWGR-based beam-steering module,<sup>[16,17]</sup> a liquid-crystal polarization controller, and a metasurface polarization beam splitter.  $M \times N$  outputs of the AWGR are connected to an  $M \times N$  2D fiber array. The output plane of the fiber array is placed in the object plane of a half lens. The output beams of the fiber array are first modulated by the liquid-crystal polarization controller to manipulate their polarization, following which they are deflected by the half lens. The deflected beams are then reflected by the metasurface polarization beam splitter, which is placed in the focal plane of the half lens. Both normal reflection and abnormal reflection occur on the surface of the metasurface polarization beam splitter; thus, the number of final output beams is doubled, and the total beam coverage area is greatly expanded (normal reflection coverage + abnormal reflection coverage).

The proposed beam-steering system has two tuning schemes: wavelength tuning and polarization tuning. By adjusting the input wavelength of the AWGR, one can control the position of the lighted fiber and then control the beam direction after the half lens, which further controls the emission directions of a pair of normally and abnormally reflected output beams. The polarization tuning is enabled by the liquid-crystal polarization controller and the metasurface polarization beam splitter. For a  $y$ -polarized incident beam, the metasurface polarization beam splitter generates a positive phase gradient along the negative  $x$ -direction; thus, the beam is abnormally reflected, as shown in **Figure 1**. The nonlinear relation between the abnormal reflection angle  $\theta_r$  and the incident angle  $\theta_i$  is  $\sin \theta_r = \sin \theta_i + \lambda/\Lambda$ , where  $\lambda$  is the wavelength and  $\Lambda$  is the length of the super cell of the metasurface polarization beam splitter, as shown in **Figure 1**. The  $\theta_r - \theta_i$  relation implies a critical incident angle  $\theta_{ic} = \arcsin(1 - \lambda/\Lambda)$ . For an  $x$ -polarized incident beam, the metasurface polarization beam splitter acts as a mirror, and the beam is normally reflected. By adjusting the polarization of a fiber beam with the liquid-crystal polarization controller, one can control the power distribution between the corresponding normally and abnormally reflected output beams. Therefore, a wavelength-polarization-controlled 2D beam-steering approach is achieved.

In Section 3, the system configuration is thoroughly discussed. The design and characterization of the metasurface

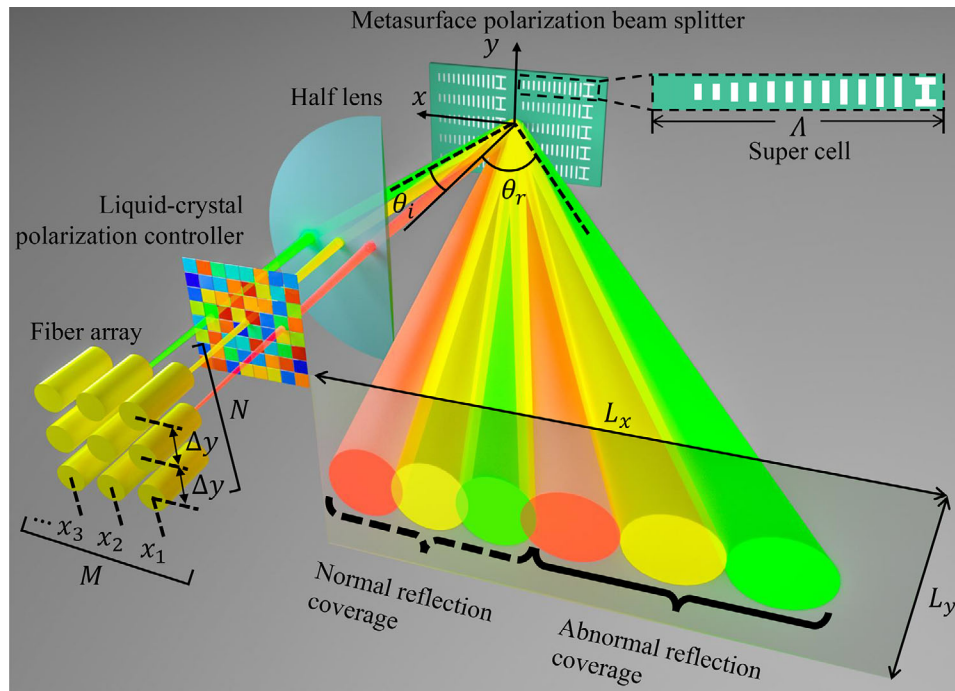


**Figure 1.** Architecture of the proposed metasurface-based 2D IR beam-steering system.

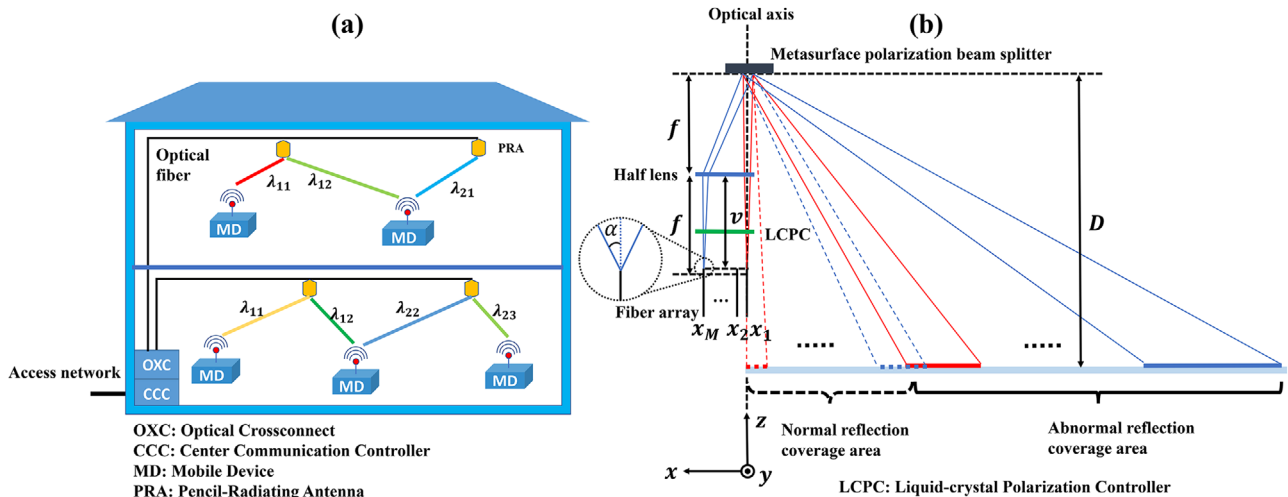


**Figure 2.** a) Indoor beam-steered infrared light communication network. b) Schematic of the proposed 2D beam-steered infrared wireless communication system.

polarization beam splitter are presented in detail in Sections 4 and 5, respectively.

### 3. System Design

The concept of the indoor beam-steered infrared light communication network is shown in **Figure 2a**.<sup>[17]</sup> In each room, several pencil-beam radiating antennas can provide high-speed connections to mobile devices with well-directed narrow IR beams. To cover the whole area, 2D IR beam steering is essential.

**Figure 2b**, which is the  $\gamma = 0$  cross section of **Figure 1**, schematically illustrates the configuration of the proposed 2D IR beam-steering system. The fiber array is placed away from the focus and closer to the lens. The distance between the output plane of the fiber array and the half lens is  $v$ , which defines the relative defocusing parameter  $p = 1 - v/f$  ( $0 \leq p < 1$ ). The metasurface polarization beam splitter is placed in the focal plane of the half lens. Here, the half lens is used to avoid blocking the reflected beams.

The system aims to cover a square image area of size  $L_x \times L_y$  with no spacing between adjacent beam spots, as shown in

Figure 1. Since the positive phase gradient of the metasurface polarization beam splitter is along the negative  $x$ -direction, the wave vector in the  $y$ -direction follows the law of specular reflection. Therefore, in the  $y$ -direction, the nonlinearity of the abnormal reflection is not significant, and the system can be configured by only considering the normal reflection coverage. Each beam spot has the same width  $W_y$  in the normal reflection coverage area. To cover a length of  $L_y$  at a distance  $D$  from the metasurface while no spacing exists between adjacent beam spots,  $W_y$  should be equal to  $L_y/N$ . The required lens focal length  $f$  and the constant  $y$ -direction fiber spacing  $\Delta y$  can be determined by using paraxial geometric optics<sup>[16]</sup>

$$f = \frac{L_y}{N \times 2 \tan \alpha} - p \times D \quad (1)$$

$$\Delta y = 2f \times \tan \alpha \times \left( \frac{f}{D} + p \right) \quad (2)$$

where  $\tan \alpha = \lambda/(\pi w_0)$  with the mode field radius  $w_0$  of the single-mode fiber. In the normal reflection coverage area, the beam spots are all round. If the  $x$ -direction fiber spacing  $\Delta x$  is constant and equal to  $\Delta y$ , the normal reflection area can be just covered. However, in this case, owing to the nonlinearity of the abnormal reflection, the abnormal-reflection coverage area cannot be fully covered. Thus, the position of each column of the fiber array  $x_1, x_2 \dots$  should be determined by making the beam spots of adjacent fiber columns tangential along the  $x$ -direction in the abnormal reflection coverage area

$$\begin{aligned} & D \times \tan \left\{ \arcsin \left\{ \sin \left[ \arctan \left( \frac{x_{n+1} - pf \times \tan \alpha}{f} \right) \right] + \frac{\lambda}{\Lambda} \right\} \right\} \\ & - f \times \tan \alpha \\ & = D \times \tan \left\{ \arcsin \left\{ \sin \left[ \arctan \left( \frac{x_n + pf \times \tan \alpha}{f} \right) \right] + \frac{\lambda}{\Lambda} \right\} \right\} \\ & + f \times \tan \alpha \end{aligned} \quad (3)$$

where  $n = 1, 2 \dots$ ,  $\lambda$  is the wavelength and  $\Lambda$  is the length of the super cell of the metasurface polarization beam splitter.  $x_n$  ( $n \geq 2$ ) can be obtained from the recursive formula (3) with the initial condition  $x_1 = 0$ .

A condition on  $x_M$  is still needed to determine where to stop (i.e., the value of  $M$ ). This condition can be obtained from the situation in which the normal and abnormal reflection coverage areas exactly overlap

$$\begin{aligned} & f \times \tan \left\{ \arcsin \left\{ \sin \left[ \arctan (-p \times \tan \alpha) \right] + \frac{\lambda}{\Lambda} \right\} \right\} - \frac{2f^2 \times \tan \alpha}{D} \\ & - pf \times \tan \alpha \leq x_M < \\ & f \times \tan \left\{ \arcsin \left\{ \sin \left[ \arctan (p \times \tan \alpha) \right] + \frac{\lambda}{\Lambda} \right\} \right\} \\ & - pf \times \tan \alpha \end{aligned} \quad (4)$$

$x_M$  should take the minimum value in this range. On the other hand,  $x_M$  is also limited by the critical angle of the metasurface polarization beam splitter

$$x_M < f \times \tan(\theta_{ic}) - pf \times \tan \alpha \quad (5)$$

where  $\theta_{ic} = \arcsin(1 - \lambda/\Lambda)$  is the critical angle of the metasurface polarization beam splitter. Based on the above two formulas, the following condition should be satisfied to ensure that no gap exists between the normal and abnormal reflection coverage areas:

$$\sin[\arctan(p \times \tan \alpha)] < 1 - \frac{2\lambda}{\Lambda} \quad (6)$$

Since  $p \times \tan \alpha$  is usually small ( $\approx 10^{-2}$ ), a clearer relation can be obtained by ignoring it

$$\Lambda > 2\lambda \quad (7)$$

which is the design requirement for the metasurface polarization beam splitter. With the value range of  $x_M$  and the initial condition  $x_1 = 0$ , the number of the fiber columns  $M$  and the  $x$ -position of each column  $x_1, x_2 \dots x_M$  can be fully determined by using the recursive formula (3). Furthermore, the coverage length in the  $x$ -direction can now be obtained

$$\begin{aligned} L_x = D \times \tan \left\{ \arcsin \left\{ \sin \left[ \arctan \left( \frac{x_M + pf \times \tan \alpha}{f} \right) \right] + \frac{\lambda}{\Lambda} \right\} \right\} \\ + f \times \tan \alpha \end{aligned} \quad (8)$$

In the abnormal reflection coverage area, no spacing or overlap exists between adjacent beam spots. In the normal reflection coverage area, no spacing or overlap exists between adjacent beam spots along the  $y$ -direction, while an overlap exists between adjacent beam spots along the  $x$ -direction because the distance between two fiber columns is less than  $\Delta y$ . A square image area of size  $L_x \times L_y$  is fully covered. In practice, due to the wavelength tuning, slight wavelength difference exists between the beams emitted from different fibers. The maximum wavelength difference is usually tens of nanometers, which is two orders of magnitude smaller than the wavelengths in fiber-optic communication. Considering  $\Lambda > 2\lambda$ , the influence of wavelength change can be ignored, and the reflection characteristics of the metasurface can be considered the same for all the wavelengths. Therefore, the system can be configured at one wavelength (usually at the center wavelength), as done in the design process above.

As an example, we use the same basic parameters as Koonen et al.<sup>[16]</sup>:  $p = 0.21$ ,  $L_y = 1.68$  m,  $D = 2.4488$  m,  $N = 14$ ,  $\lambda = 1.5$   $\mu\text{m}$ , and  $w_0 = 4.5$   $\mu\text{m}$ . In our metasurface polarization beam splitter,  $\Lambda = 4$   $\mu\text{m}$ , which meets  $\Lambda > 2\lambda = 3$   $\mu\text{m}$ . Then, we find  $f = 51.2$  mm,  $\Delta y = 2.51$  mm,  $M = 9$ ,  $L_x = 2.75$  m, and  $x_M = 19.4$  mm. Therefore, an image area of  $2.75 \times 1.68$  m<sup>2</sup> is fully covered with a  $9 \times 14$  2D fiber array (126-port AWGR), the total size of which is  $19.4 \times 32.63$  mm<sup>2</sup>. Compared with the demonstration by Koonen et al.<sup>[16]</sup> in which  $1.68 \times 1.68$  m<sup>2</sup> is fully covered with a  $14 \times 14$  2D fiber array (196-port AWGR) of total size  $32.63 \times 32.63$  mm<sup>2</sup>, our system is considerably enhanced in coverage and size while using the same basic parameters.

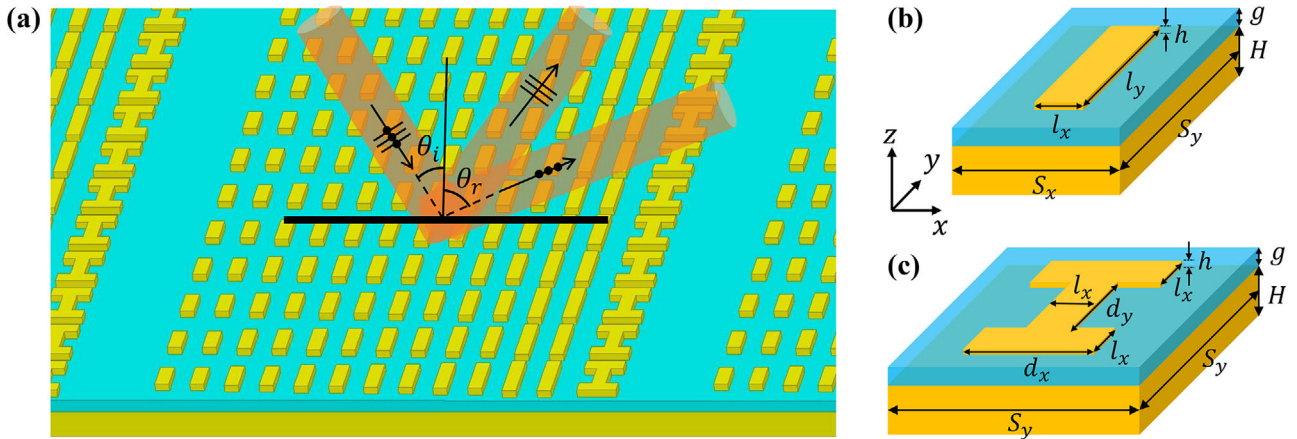


**Figure 3.** a) Schematic of the designed polarization beam splitter.  $\theta_i$  is the incident angle, and  $\theta_r$  is the abnormal reflection angle (in the  $xz$ -plane). b) Schematic of the type 1 meta-atom. c) Schematic of the type 2 meta-atom.

#### 4. Device Design

The metasurface polarization beam splitter plays a key role in the proposed 2D IR beam-steering system. Here, to demonstrate the system concept, a GSPM-based metasurface polarization beam splitter is designed and fabricated at  $\lambda = 1550$  nm. **Figure 3a** schematically shows the designed polarization beam splitter, which consists of periodical arrays of gap plasmon-based meta-atoms. Two types of meta-atoms are used, type 1 and type 2, as shown in **Figure 3b,c**, respectively. They are both composed of an Au ground, a  $\text{SiO}_2$  spacer in the middle, and a top Au nano-pattern designed with different shapes. When the meta-atom is illuminated by an  $x$ -polarized or a  $y$ -polarized incident plane wave, electric currents are induced on both the top Au pattern and the bottom Au ground, which result in strong near-field coupling and anti-parallel electric current oscillations, forming strong magnetic resonance.<sup>[37]</sup> By varying the geometry of the meta-atoms, the reflection phase and amplitude of each unit cell can be engineered independently at the designed wavelength.

All the design parameters are optimized by using Lumerical finite-difference time-domain (FDTD) software. The software in-built material database is used to build the structures. In the simulation of each meta-atom, periodic boundary conditions are applied on the four sides ( $yz$  and  $xz$ -planes) of the structure. Perfectly matched layer (PML) boundaries are applied on the top and bottom of the simulation box. A normally incident plane wave source at 1550 nm is used as illumination.

As shown in **Figure 4a**, a super cell consists of eight phase units is designed to cover a  $2\pi$  phase with a  $\pi/4$  phase interval. Each phase unit is made of meta-atoms with different geometries. In our design, all the meta-atoms share the following parameters:  $S_x = 250$  nm,  $S_y = 500$  nm,  $H = 200$  nm,  $g = 90$  nm,  $l_x = 100$  nm, and  $h = 55$  nm. The zero-phase unit has no Au pattern on the  $\text{SiO}_2$  spacer. Each of the six phase units from  $\pi/4$  to  $6\pi/4$  is a parallel connection of two identical type-1 meta-atoms. The pattern lengths  $l_y$  are 225 nm, 266 nm, 292 nm, 315 nm, 345 nm, and 413 nm, respectively. The  $7\pi/4$  phase unit is a single type-2 meta-atom with  $d_x = 280$  nm and  $d_y = 200$  nm.

Compared with the design wavelength  $\lambda = 1550$  nm, all the meta-atoms have subwavelength dimensions.

**Figure 4b** shows the simulated scattered  $E_y$  phase patterns of all the phase units in a super cell under the illumination of a normally incident  $y$ -polarized plane wave ( $\lambda = 1550$  nm). It can be seen that a positive phase gradient along the  $x$ -direction is formed, which creates an abnormal reflected wavefront. According to the generalized laws of reflection and refraction,<sup>[38]</sup> for a  $y$ -polarized plane wave at an incident angle  $\theta_i$ , the abnormal reflection angle  $\theta_r$  is

$$\sin \theta_r = \sin \theta_i + \frac{\lambda}{\Lambda} \quad (9)$$

where  $\Lambda$  is the length of the super cell. In our design,  $\Lambda = 4 \mu\text{m}$ . It can be seen that  $\theta_i$  and  $\theta_r$  have a nonlinear relation, and a critical angle exists for  $\theta_i$ :

$$\theta_{ic} = \arcsin \left( 1 - \frac{\lambda}{\Lambda} \right) \quad (10)$$

When  $\theta_i > \theta_{ic}$ , the abnormal reflection disappears, and surface plasmon-polaritons are excited. To obtain a broad incident range and meet the design requirement  $\Lambda > 2\lambda$ , a large  $\theta_{ic}$  is needed, resulting in a large  $\Lambda$ . Therefore, eight phase units are used to cover  $2\pi$  ( $\theta_{ic} = 37.77^\circ$ ) with a  $\pi/4$  phase interval. However, the  $\pi/4$  phase interval cannot be achieved using only type-1 meta-atoms; therefore, type-2 meta-atom is introduced to achieve a large phase shift.

**Figure 4c** precisely shows the scattered phase of each phase unit, which uniformly covers a  $2\pi$  phase. The simulation results agree very well with the model. The reflectivity of each phase unit is shown in **Figure 4d**, overall good efficiency is obtained. **Figure 5** further shows the simulated  $xy$ -plane electric-field magnitude distribution in the center of the spacer of the designed meta-atoms. It can be seen that similar resonances occur in each meta-atom, and the resonance can be manipulated by varying the length of the top Au nano-pattern. Therefore, different phase

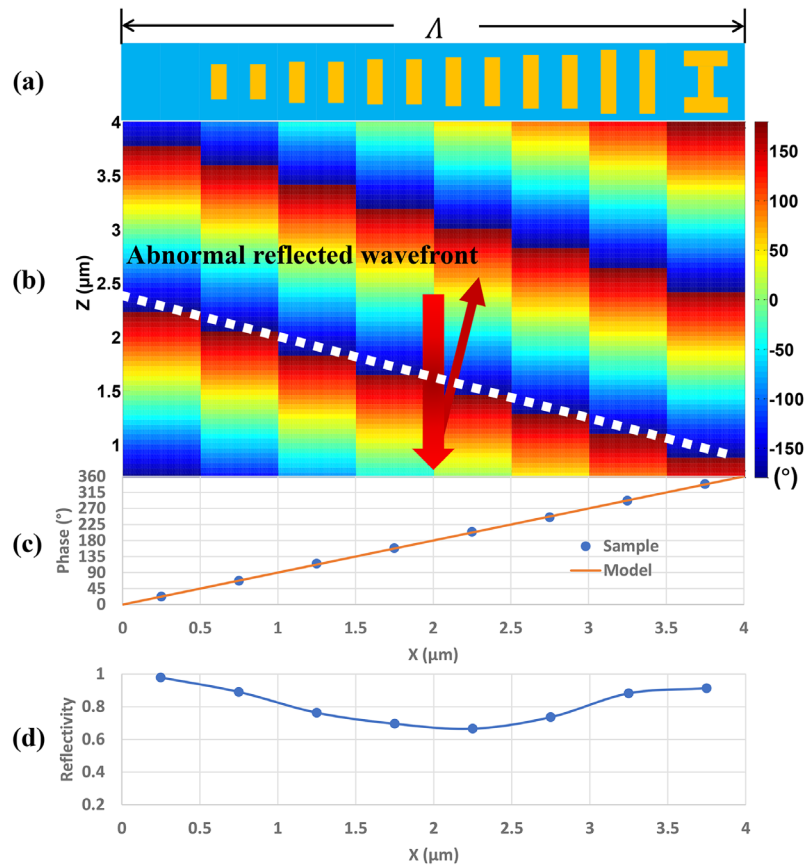


**Figure 4.** a) Super cell of the designed metasurface polarization beam splitter. b) Simulated scattered  $E_y$  phase patterns of all the phase units under the illumination of a normally incident y-polarized plane wave ( $\lambda = 1550$  nm). c) Scattered phase of each phase unit within a super cell. d) Reflectivity of each phase unit within a super cell.

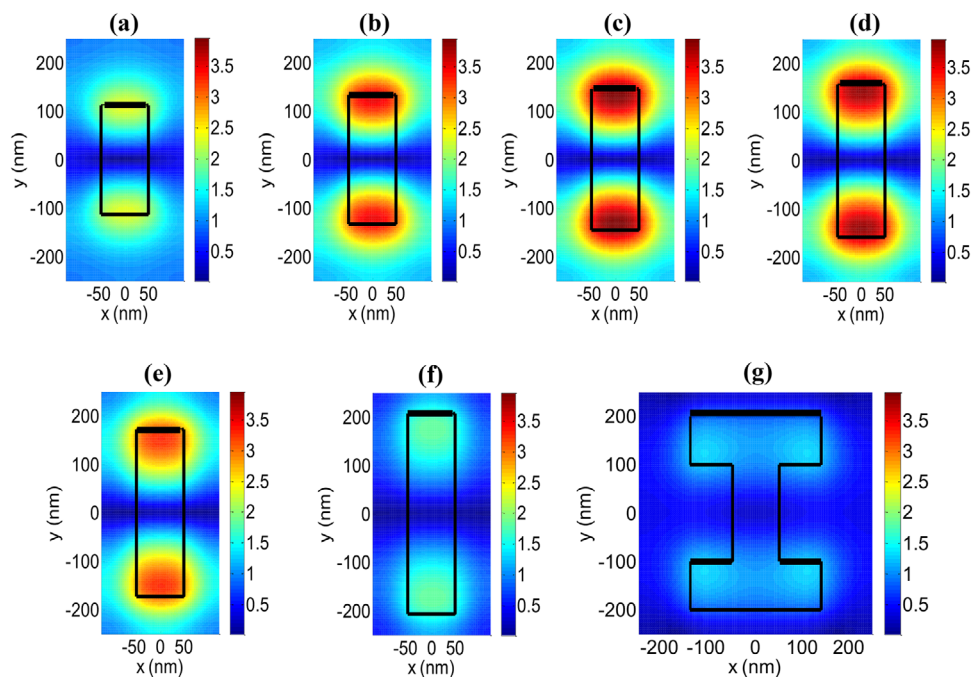


**Figure 5.** Magnitude of the electric field at  $\lambda = 1550$  nm in the xy-plane in the center of the spacer, under a normally incident y-polarized plane wave. Panels a–f) correspond to  $l_y = 225, 266, 292, 315, 345,$  and  $413$  nm type-1 meta-atoms, respectively. Panel g) corresponds to the type-2 meta-atom.

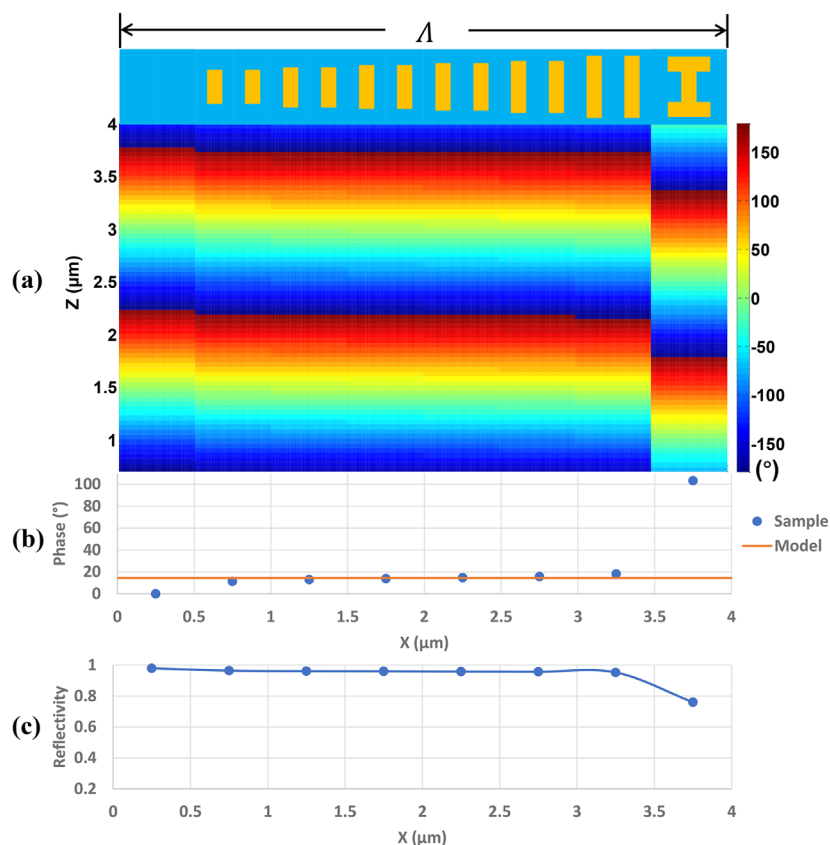


**Figure 6.** a) Simulated scattered  $E_x$  phase patterns of all the phase units in a super cell under the illumination of a normally incident  $x$ -polarized plane wave ( $\lambda = 1550$  nm). b) Scattered phase of each phase unit within a super cell. c) Reflectivity of each phase unit within a super cell.

responses can be obtained. Combined with Figure 4d, we can find that stronger coupling leads to lower reflectivity.

For an  $x$ -polarized incident plane wave, the phase response of each phase unit is basically the same. **Figure 6a** shows the simulated scattered  $E_x$  phase patterns of all the phase units in a super cell under the illumination of a normally incident  $x$ -polarized wave ( $\lambda = 1550$  nm). The corresponding phase values are shown in **Figure 6b**. Since two types of meta-atoms are used, a phase mismatch exists as we can see in **Figure 6a**. However, most of the phase units have the same phase response. Thus, in general, the super cell acts as a mirror. The reflectivity of each phase unit is shown in **Figure 6c**; high efficiency is obtained.

Based on the above discussions, the designed metasurface has different reflection characteristics for  $x$  and  $y$ -polarized incident light, that is, a polarization beam splitter. With this polarization beam splitter, one can manipulate the direction and power of the reflected light by controlling the polarization of the incident light.

## 5. Device Characterization and Polarization-Controlled 2D Beam Steering

A metasurface polarization beam splitter was fabricated in our clean room, as shown in **Figure 7**. In the previous section, the metasurface is designed and optimized under the illumination of

normally incident  $x$  and  $y$ -polarized plane waves at  $\lambda = 1550$  nm. In addition, the discussed incident beams are limited in the  $xz$ -plane as shown in **Figures 1, 2b, and 3a**. These analyses are enough for system and device design. However, to support the ideal of polarization-wavelength-controlled 2D IR beam-steering, more solid proof is needed. Therefore, the fabricated metasurface is fully measured under comprehensive incident, as schematically shown in **Figure 8**. The incident direction is described by two angles: the azimuthal angle  $\eta$ , and the polar angle  $\gamma$ , as defined in **Figure 8**. Because of the symmetry of the designed metasurface,  $\eta$  can be limited to  $0^\circ$  to  $90^\circ$ . We did comprehensive measurements in five incident planes:  $\eta = 0^\circ, 20^\circ, 45^\circ, 65^\circ,$  and  $90^\circ$ . In each incident plane,  $\gamma$  is set within  $0^\circ$  to  $35^\circ$ . Because wavelength tuning is applied in the system, all measurements are performed at three wavelengths: 1530, 1550, and 1565 nm, corresponding to the C band.

By using a charge-coupled device image sensor, the far-field beam spots of the normal and abnormal reflection are observed in the  $xz$ -plane ( $\eta = 0^\circ$ ) with different incident angles ( $\gamma$ ), as shown in **Figure 9**. Here, the incident beams are collimated to have small divergence angles and the incident beam spots are shown as reference. All the beam spots are observed at the same distance from the light source. For the abnormal reflection, the beam spots slowly change from circular to oval-like as the incident angle ( $\gamma$ ) increases. This is due to the nonlinearity of the abnormal reflection, which makes the beam diverge faster in



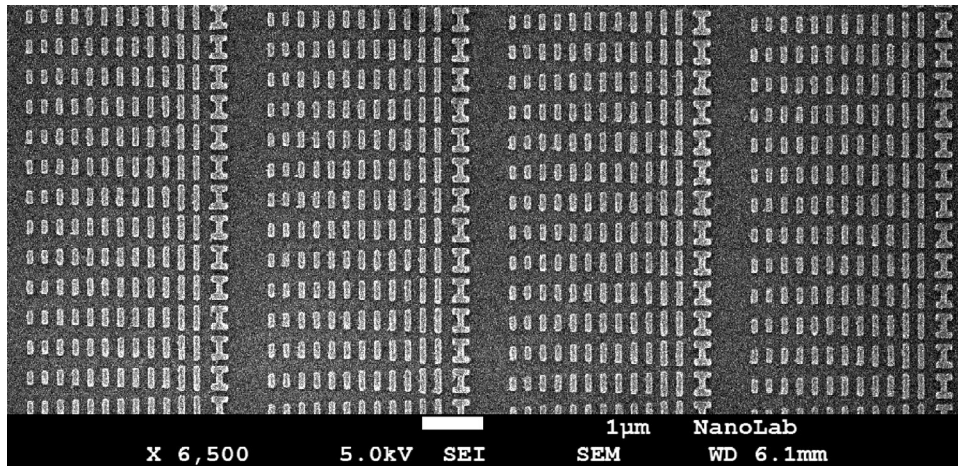


Figure 7. SEM image of the fabricated metasurface polarization beam splitter.

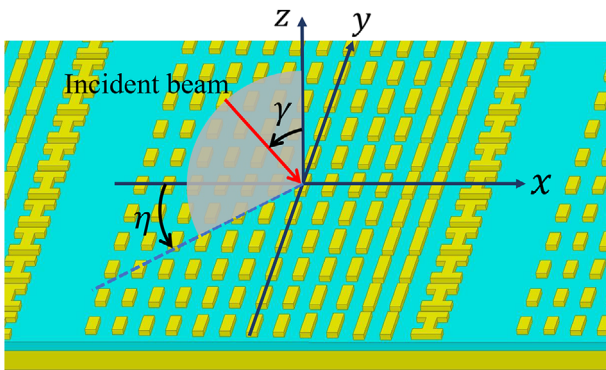


Figure 8. Schematic of the incident direction in the device measurements.

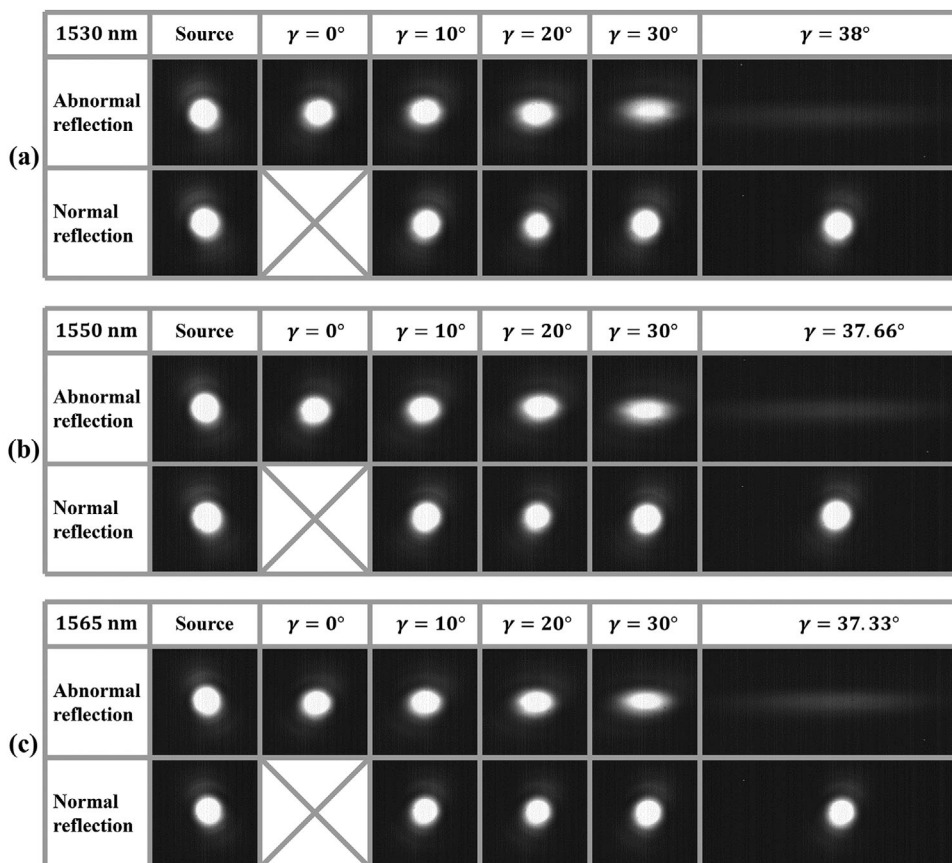
the  $x$ -direction than in the  $y$ -direction. To observe the abnormal reflection closing to the critical angles,  $\gamma$  is set to  $38^\circ$ ,  $37.66^\circ$ , and  $37.33^\circ$  at 1530, 1550, and 1565 nm, respectively. The critical angles at the three wavelengths are  $38.13^\circ$ ,  $37.77^\circ$ , and  $37.49^\circ$ , respectively. It can be seen the observed beam spots are severely stretched, and the abnormal reflection almost disappear, which is as expected. We can also find that the beam distortion is slight when the incident angle ( $\gamma$ ) is away from the critical angle, while severe distortion occurs when the incident angle ( $\gamma$ ) is close to the critical angle, because the nonlinearity of the abnormal reflection is significant in this case. For the normal reflection, all the observed beam spots maintain basically unchanged as the incident angle ( $\gamma$ ) increases, which prove that the designed metasurface does act like a mirror in this situation.

Figure 10 shows the measured relation between the incident angle and the abnormal reflection angle. These angle relations are measured in the  $xz$ -plane ( $\eta = 0^\circ$ ). It can be seen that the measurement results agree very well with the theory and the simulation results. The angle relation remains almost unchanged when the input wavelength switches from 1530 to 1565 nm, which is compatible with the proposed 2D IR beam-steering system.

To prove the feasibility of the proposed polarization-wavelength-controlled 2D IR beam steering, we measured the power imbalance between the normal and abnormal reflec-

tion at different incident polarization states and wavelengths, as shown in Figure 11a–c. The measurements are performed in the five incident planes (defined by  $\eta$ ). In each incident plane, three incident polar angles are set:  $\gamma = 10^\circ$ ,  $20^\circ$ , and  $30^\circ$ . Here, the power imbalance is defined as the received optical power (in dBm) of the abnormal reflection minus that of the normal reflection. It can be seen at all the three wavelengths, when the polarization state changes by  $90^\circ$ , the beam power switches from the abnormal reflection direction to the normal reflection direction, and vice versa. The maximum and minimum power imbalance indicates the isolation between the normal and abnormal reflection. The polarization state that maximizes the abnormal reflection (or normal reflection) shifts as the incident plane changes. We also measured the total efficiency of the normal and abnormal reflection, as shown in Figure 11d–f. High power efficiency ( $>67\%$ ) is achieved at all the polarization states and wavelengths. Polarization-controlled 2D beam steering is verified in a broad wavelength band, which gives good proof to the proposed 2D beam steering system.

The power efficiency of the normal and abnormal reflection is also measured in the five incident planes with different incident polar angles ( $\gamma$ ), as shown in Figure 12. The measurements start from  $\gamma = 10^\circ$  because the normal reflection is blocked by our measurement setup when  $\gamma < 10^\circ$ . The power efficiency of the abnormal reflection (normal reflection) is measured by adjusting the incident polarization to maximize the received abnormal reflection (normal reflection) power while keeping the incident power constant. At all the three wavelengths, the measured results show similar trends. For the abnormal reflection, the reflection efficiency decreases gently with increasing  $\gamma$ . The measured efficiency is  $\approx 80\%$  when  $\gamma$  is less than  $15^\circ$  in all the incident planes and wavelengths, and it is  $>70\%$  when  $\gamma$  is less than  $25^\circ$ , which is state-of-the-art efficiency. For the normal reflection, in all the incident planes and wavelengths, the measured reflection efficiency is  $>75\%$  for most of the  $\gamma$ . It can be seen when  $\eta = 0^\circ$ ,  $20^\circ$ ,  $45^\circ$ , and  $65^\circ$ , there are efficiency notches at some specific  $\gamma$ , where the efficiency drops to around 60%. This is caused by the angular dispersion under TM-polarized illumination.<sup>[39]</sup> When  $\eta = 90^\circ$ , there is no efficiency notch. Because in this case, the incident wave that maximizes the normal reflection is a TE wave.



**Figure 9.** Measured far-field beam spots of the normal and abnormal reflection in the  $xz$ -plane ( $\eta = 0^\circ$ ) with different incident angles ( $\gamma$ ). Panels a–c correspond to  $\lambda = 1530, 1550,$  and  $1565$  nm, respectively.

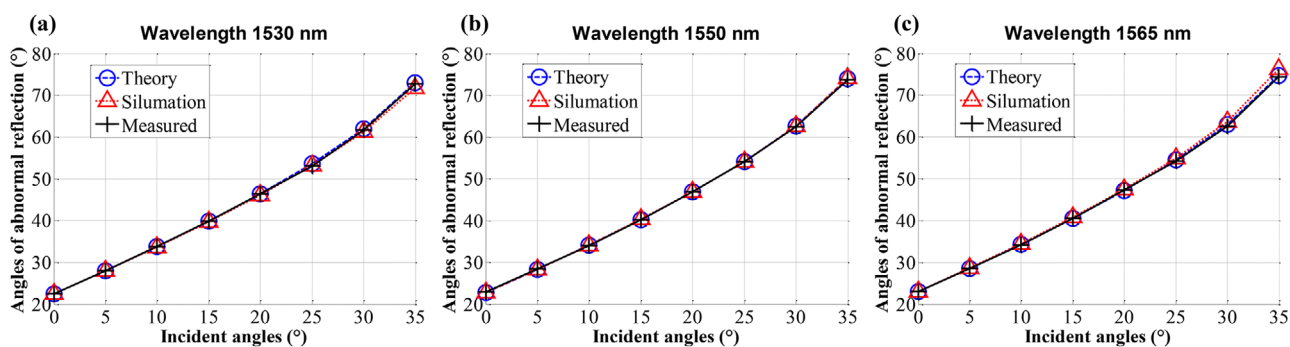


**Figure 10.** Measured relation between the incident angle and the abnormal reflection angle. The measurements are performed in the  $xz$ -plane ( $\eta = 0^\circ$ ). Panels a–c correspond to  $\lambda = 1530, 1550,$  and  $1565$  nm, respectively.

In general, the influence of the angular dispersion is limited, and a high reflection efficiency is achieved. The simulation results at  $\eta = 0^\circ$  are also presented in Figure 12. The trend of the simulated curves matches that of the measured curves. For the efficiency of the abnormal reflection, good agreement is achieved between the simulation and the measurement, especially when  $\gamma < 30^\circ$ . For the efficiency of the normal reflection, the position of the efficiency notches is also matched. The difference between the simulation and the measurement mainly comes

from the fabrication error, the material property difference between the simulation database and the actually used materials, and the simulation accuracy. Nevertheless, the simulation results do show the important characteristics of the fabricated metasurface.

The isolation between the normal and abnormal reflection is measured in the same manner as the efficiency. As shown in Figure 13, the isolation shows the similar trends as the efficiency. The overall abnormal to normal isolation decreases

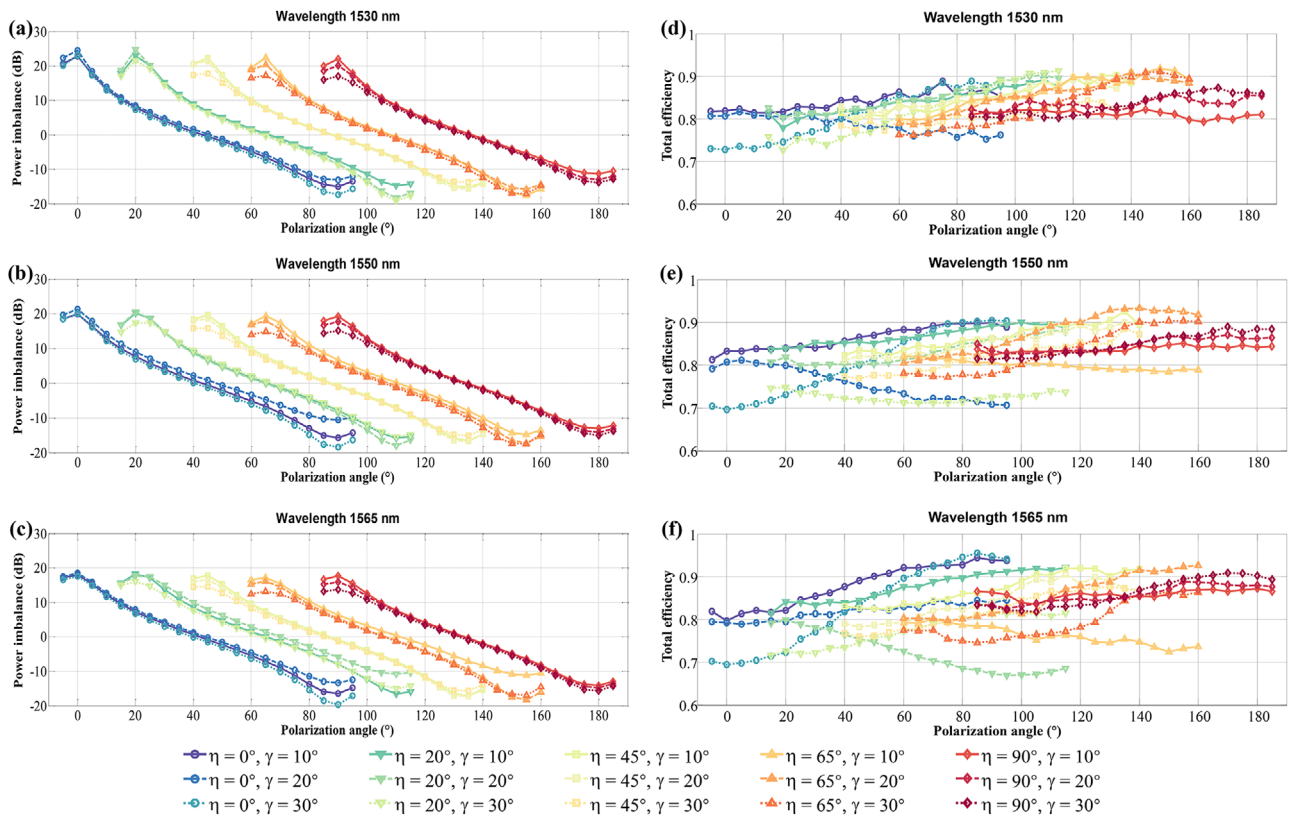


**Figure 11.** a–c) Measured power imbalance changing with incident polarization states, at  $\lambda = 1530, 1550,$  and  $1565$  nm, respectively. d–f) Measured total efficiency changing with incident polarization states, at  $\lambda = 1530, 1550,$  and  $1565$  nm, respectively. The measurements are performed in the five incident planes:  $\eta = 0^\circ, 20^\circ, 45^\circ, 65^\circ,$  and  $90^\circ$ . In each incident plane, three incident polar angles are set:  $\gamma = 10^\circ, 20^\circ,$  and  $30^\circ$ .

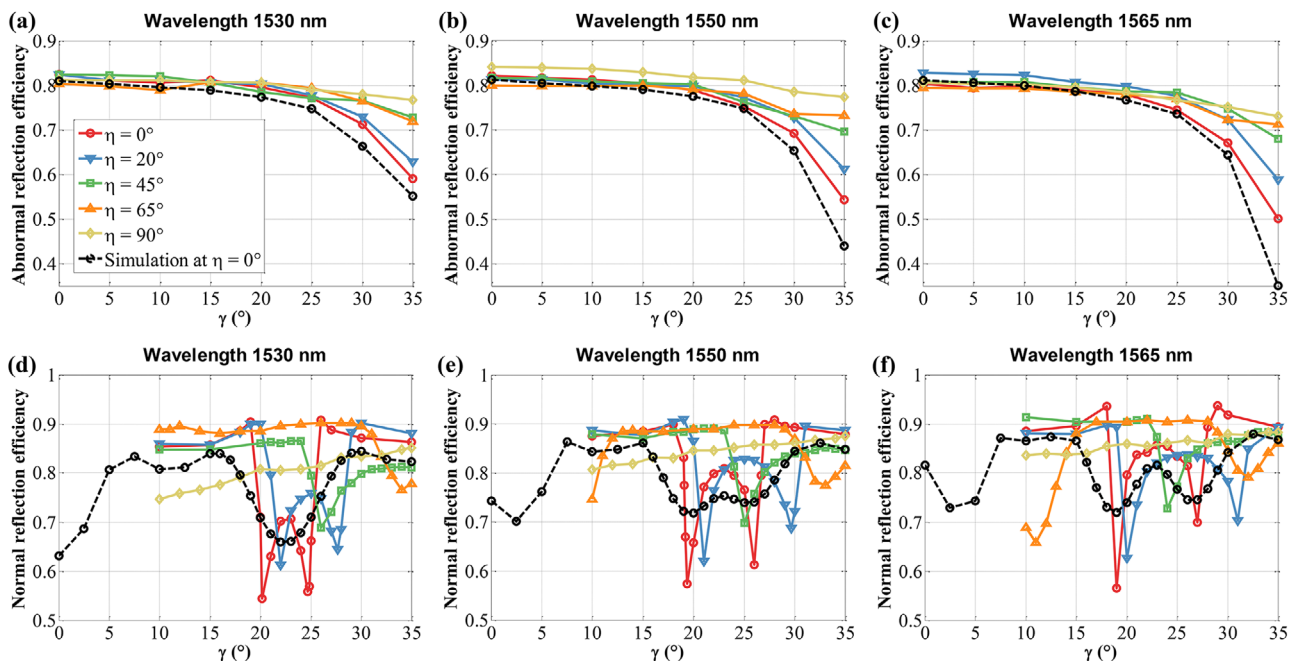


**Figure 12.** Measured power efficiency of the abnormal reflection a–c) and normal reflection d–f), at  $\lambda = 1530, 1550$  nm, and  $1565$  nm, respectively. The measurements are performed in the five incident planes:  $\eta = 0^\circ, 20^\circ, 45^\circ, 65^\circ,$  and  $90^\circ$ . Simulation results at  $\eta = 0^\circ$  are also presented.

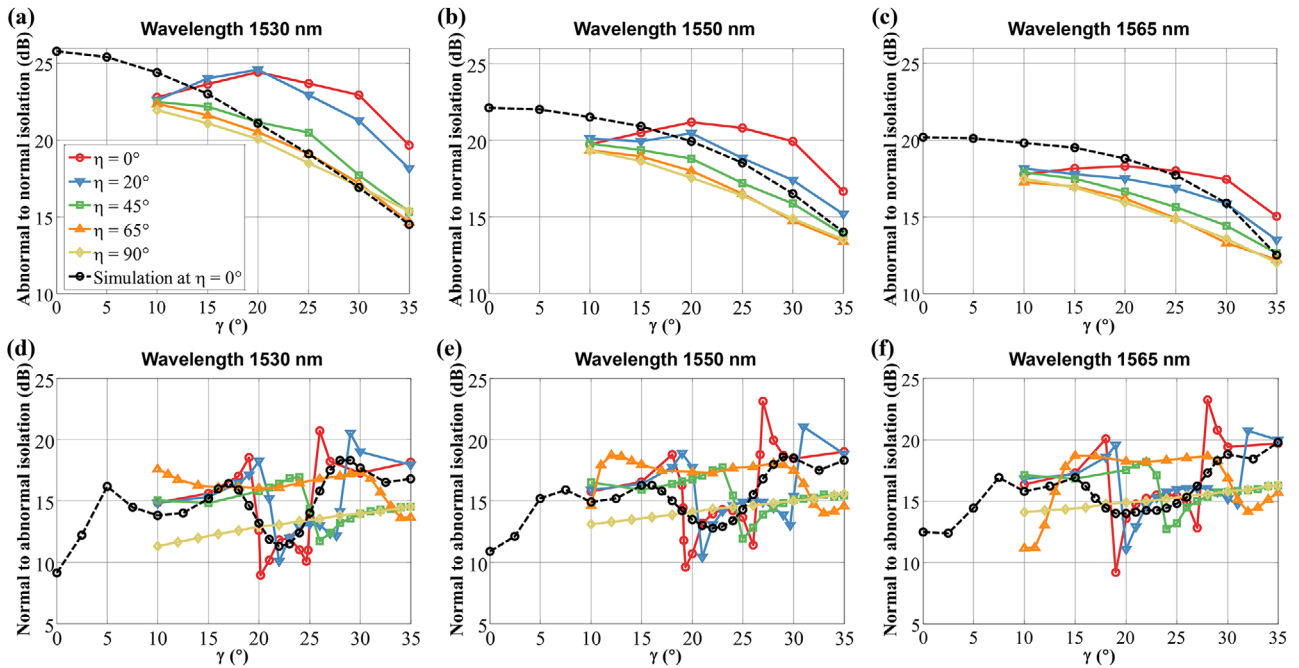


**Figure 13.** a–c) Measured abnormal to normal isolation, at  $\lambda = 1530, 1550,$  and  $1565,$  respectively. d–f) Measured normal to abnormal isolation, at  $\lambda = 1530, 1550,$  and  $1565$  nm, respectively. The measurements are performed in the five incident planes:  $\eta = 0^\circ, 20^\circ, 45^\circ, 65^\circ,$  and  $90^\circ.$  Simulation results at  $\eta = 0^\circ$  are also presented.

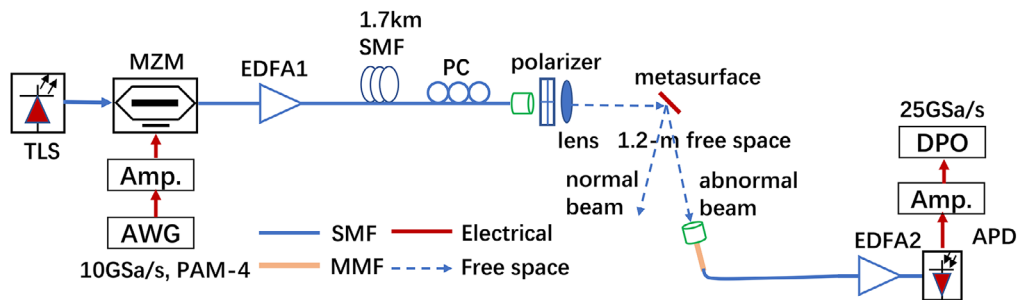


**Figure 14.** Experimental setup of the metasurface-based beam-steered infrared wireless link. TLS, tunable laser source; AWG, arbitrary waveform generator; MZM, Mach–Zehnder modulator; EDFA1, erbium-doped fiber amplifier; SMF, single-mode fiber; PC, polarization controller; APD, avalanche photodiode; DPO, digital phosphor oscilloscope.

from  $20 \pm 5$  dB to  $15 \pm 3$  dB as the wavelength increases from 1530 to 1565 nm. The overall normal to abnormal isolation is  $15 \pm 5$  dB at all the three wavelengths. Isolation notches can be seen in Figure 13d–f, which is caused by the efficiency notches of the abnormal reflection. The isolation can also be obtained from the maximum and minimum values of a power imbalance curve shown in Figure 11, but only for  $\gamma = 10^\circ, 20^\circ,$  and  $30^\circ.$  The simulation results at  $\eta = 0^\circ$  are also presented in Figure 13.

The measurement results prove the abnormal reflection characteristics and the good performance of the designed metasurface polarization beam splitter in a broad bandwidth from 1530 nm to 1565 nm (C band). The device has a large incident angle range and a high reflection efficiency. When the incident polar angle ( $\gamma$ ) changes from  $0^\circ$  to  $35^\circ,$  the efficiency (for both normal and abnormal reflection) is larger than 50% (3 dB). An

incident polar angle of up to  $35^\circ$  is available, which is close to the critical angle ( $37.77^\circ$  at 1550 nm when  $\eta = 0^\circ$ ). Polarization-controlled 2D IR beam-steering is also verified by changing the polarization states of incident beams in multiple incident planes and polar angles. Therefore, the feasibility of the proposed 2D IR beam-steering system is verified.

## 6. System Demonstration

A proof-of-concept experimental setup was built using the fabricated metasurface, as shown in Figure 14. A tunable laser source with a 10-dBm output optical power is used to generate the optical carrier in the communication control center, which is then modulated by a 10-GHz Mach–Zehnder modulator (MZM). The electrical data are produced by an arbitrary waveform generator

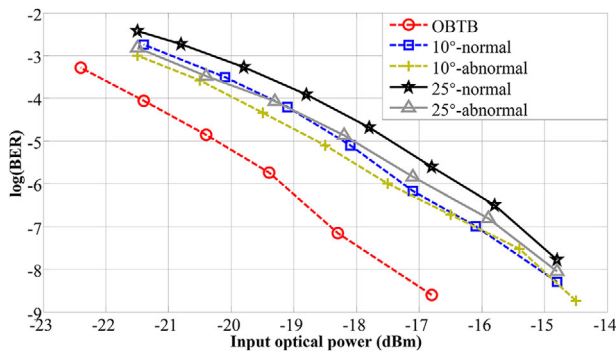


**Figure 15.** BER performance of a 10-Gbaud  $s^{-1}$  PAM4 signal over 1.2-m free space at incident angles  $\gamma = 10^\circ$  and  $25^\circ$ . The measurements are performed in the  $xz$ -plane ( $\eta = 0^\circ$ ), and  $\lambda = 1550$  nm.

(AWG) to drive the MZM after amplification. In the experiment, transmitted pulse amplitude modulation (PAM) signals are generated offline using a MATLAB program and then sampled by the AWG running at  $10 \text{ GSa } s^{-1}$ , producing a  $10 \text{ Gbaud } s^{-1}$  PAM-4 baseband signal. Thus, the achieved data rate is 20 Gbps. It is worth noting that the data rate is limited by the used optoelectronic devices. If a large bandwidth transceiver is employed, 100 Gbps data rate or more can be achieved. Moreover, the insertion loss caused by the designed metasurface chip is less than 3 dB, which enables to achieve high signal-to-noise-ratio values to meet the high-speed transmission requirement. The received electrical PAM-4 signal is oversampled by the digital phosphor oscilloscope (DPO) sampling at  $25 \text{ GSa } s^{-1}$ . The modulated optical signal is amplified by an erbium-doped fiber amplifier (EDFA) and then launched into a 1.7-km single-mode fiber. A polarization controller combined with a free-space polarizer are used to control the polarization states of the incident light so as to manipulate the power distribution of beams emerging from the metasurface chip. The optical beam is launched into free space via a collimator (the focal length is 18 mm) with a measured power below 10 dBm which meets the requirements of human eye safety. The light is further collimated by a lens and then launched onto the chip, resulting in normal and abnormal beams. After 1.2-m free-space transmission, both beams are coupled into a short section of a multi-mode fiber and then a single-mode fiber via another collimator. The received optical power is amplified and then detected by an avalanche photodiode. The amplified output electrical signal is acquired by a DPO for further signal processing.

**Figure 15** illustrates the bit-error-ratio (BER) performance of the 20-Gbps PAM-4 signal as a function of the optical power received by a variable optical attenuator placed at the front of the avalanche photodiode. The incident beam is in the  $xz$ -plane ( $\eta = 0^\circ$ ), and the incident angles ( $\gamma$ ) are set to  $10^\circ$  and  $25^\circ$ , which correspond to a beam-steering range of  $35^\circ$  (normal reflection + abnormal reflection). Four output beams are generated, transmitted, and measured at the receiver end, as shown in Figure 15. We also measured the BER performance of the 20-Gbps PAM-4 signal at optical back-to-back (OBTB) transmission. Compared to OBTB transmission, a penalty of almost 3dB is observed at a 7% forward error correction limit of  $1 \times 10^{-3}$ , which is mainly caused by the noise figure of the EDFA at the receiver end.

## 7. Conclusion

By combining active and passive approaches, we proposed a novel 2D IR beam-steering system, which can be tuned by changing the wavelength and polarization. The polarization tuning is achieved by using a metasurface polarization beam splitter in conjunction with a liquid-crystal polarization controller. The wavelength tuning is enabled by a AWGR-based beam-steering module. The proposed system keeps all the advantages of AWGR-based beam-steering approaches, and additionally has polarization control capability. Furthermore, the grating loss existing in SLM-based and grating-based beam-steering approaches is avoided by using the metasurface. Therefore, the proposed system has scalability to support multiple beams, flexibility to steer the beam, high optical efficiency, and large coverage area. With the designed and fabricated metasurface polarization beam splitter, polarization-controlled 2D IR beam steering experiments are performed, and a 20-Gbps beam-steered IR wireless link is built, as proof-of-concept.

## 8. Experimental Section

**Sample Fabrication:** The metasurface polarization beam splitter was fabricated using the following steps. Firstly, a 200-nm Au ground was deposited on a Si substrate by metal evaporation (BVR2008FC). Secondly, a 90-nm-thick  $\text{SiO}_2$  layer was deposited on the Au ground by plasma-enhanced chemical vapor deposition (PECVD). Thirdly, a 950 PMMA A4 layer was spin-coated on the  $\text{SiO}_2$  layer. After baking on a hotplate, the sample was sent into an electron beam direct write lithography system (EBPG5150) for pattern definition. After lithography, the sample was developed in an MIBK/IPA solution and then rinsed with IPA. Fourthly, a 2-nm-thick Cr layer was deposited on the sample by metal evaporation (BVR2008FC) to improve adhesion. Subsequently, a 53-nm-thick Au layer was deposited without taking the sample out. Finally, the top Au patterns were obtained by lift-off.

## Acknowledgements

J.H. and C.L. contributed equally to the paper. This work is supported by NWO Zwaartekracht program on Integrated Nanophotonics (024.002.033); ZJU-TU/e IDEAS project; Open Fund of the State Key Laboratory of Optoelectronic Materials and Technologies (Sun Yat-sen University); Key Research and Development Program of China (2018YFE0201000).

## Conflict of Interest

The authors declare no conflict of interest.

## Keywords

gap-surface plasmon metasurfaces, optical beam steering, optical wireless communication

Received: June 24, 2020  
Revised: September 13, 2020  
Published online: November 16, 2020

[1] NCAT, Growth in the internet of things, <http://www.ncta.com/chart/growth-in-the-internet-of-things#.WsSRvubTQ00.link>

- [2] Cisco, 802.11ac: The Fifth Generation of Wi-Fi, **2018**.
- [3] T. Koonen, *J. Lightw. Technol.* **2017**, *36*, 1459.
- [4] H. Haas, L. Yin, Y. Wang, C. Chen, *J. Lightw. Technol.* **2015**, *34*, 1533.
- [5] T. Koonen, K. Mekonnen, Z. Cao, F. Huijskens, N. Q. Pham, E. Tangdiongga, *Philos. Trans. R. Soc. A* **2020**, *378*, 20190192.
- [6] Z. Cao, X. Zhang, G. Osnabrugge, J. Li, I. M. Vellekoop, A. M. Koonen, *Light: Sci. Appl.* **2019**, *8*, 1.
- [7] H. Chun, S. Rajbhandari, G. Faulkner, D. Tsonev, E. Xie, J. J. D. McKeendry, E. Gu, M. D. Dawson, D. C. O'Brien, H. Haas, *J. Lightw. Technol.* **2016**, *34*, 3047.
- [8] A. Gomez, K. Shi, C. Quintana, R. Maher, G. Faulkner, P. Bayvel, B. C. Thomsen, D. O'Brien, *J. Lightw. Technol.* **2016**, *34*, 5332.
- [9] A. Gomez, K. Shi, C. Quintana, M. Sato, G. Faulkner, B. C. Thomsen, D. O'Brien, *IEEE Photonics Technol. Lett.* **2014**, *27*, 367.
- [10] A. Gomez, C. Quintana, G. Faulkner, D. O'Brien, in *Broadband Access Communication Technologies X* (Eds: B. B. Dingel, K. Tsukamoto), SPIE Press, Bellingham, Washington DC **2016**, p. 97720Q.
- [11] K. Wang, A. Nirmalathas, C. Lim, K. Alameh, E. Skafidas, *IEEE Photonics Technol. Lett.* **2016**, *28*, 790.
- [12] T. Koonen, J. Oh, K. Mekonnen, Z. Cao, E. Tangdiongga, *J. Lightw. Technol.* **2016**, *34*, 4802.
- [13] T. Chan, E. Myslivets, J. E. Ford, *Opt. Express* **2008**, *16*, 14617.
- [14] K. Wang, Z. Yuan, E. Wong, K. Alameh, H. Li, K. Sithamparanathan, E. Skafidas, *J. Lightw. Technol.* **2018**, *37*, 619.
- [15] K. Van Acoleyen, W. Bogaerts, R. Baets, *IEEE Photonics Technol. Lett.* **2011**, *23*, 1270.
- [16] T. Koonen, A. Khalid, J. Oh, F. Gomez-Agis, E. Tangdiongga, in *2017 Opto-Electronics and Communications Conference (OECC) and Photonics Global Conference (PGC)*, IEEE, Piscataway, NJ **2017**, pp. 1–4.
- [17] T. Koonen, F. Gomez-Agis, F. Huijskens, K. A. Mekonnen, Z. Cao, E. Tangdiongga, *J. Lightw. Technol.* **2018**, *36*, 4486.
- [18] N. Yu, F. Capasso, *Nat. Mater.* **2014**, *13*, 139.
- [19] A. Nemati, Q. Wang, M. Hong, J. Teng, *Opto-Electron. Adv.* **2018**, *1*, 180009.
- [20] H. T. Chen, A. J. Taylor, N. Yu, *Rep. Prog. Phys.* **2016**, *79*, 076401.
- [21] A. M. Shaltout, V. M. Shalaev, M. L. Brongersma, *Science* **2019**, *364*, 648.
- [22] C. H. Chu, M. L. Tseng, J. Chen, P. C. Wu, Y. H. Chen, H. C. Wang, T. Y. Chen, W. T. Hsieh, H. J. Wu, G. Sun, D. P. Tsai, *Laser Photonics Rev.* **2016**, *10*, 986.
- [23] P. C. Wu, R. A. Pala, G. K. Shirmanesh, W. H. Cheng, R. Sokhoyan, M. Grajower, M. Z. Alam, D. Lee, H. A. Atwater, *Nat. Commun.* **2019**, *10*, 3654.
- [24] M. R. M. Hashemi, S. H. Yang, T. Wang, N. Sepúlveda, M. Jarrahi, *Sci. Rep.* **2016**, *6*, 35439.
- [25] Q. Ma, G. D. Bai, H. B. Jing, C. Yang, L. Li, T. J. Cui, *Light: Sci. Appl.* **2019**, *8*, 98.
- [26] F. Ding, R. Deshpande, S. I. Bozhevolnyi, *Light: Sci. Appl.* **2018**, *7*, 17178.
- [27] F. Ding, Y. Yang, R. A. Deshpande, S. I. Bozhevolnyi, *Nanophotonics* **2018**, *7*, 1129.
- [28] S. Sun, K. Y. Yang, C. M. Wang, T. K. Juan, W. T. Chen, C. Y. Liao, Q. He, S. Xiao, W. T. Kung, G. Y. Guo, L. Zhou, D. P. Tsai, *Nano Lett.* **2012**, *12*, 6223.
- [29] A. Pors, M. G. Nielsen, R. L. Eriksen, S. I. Bozhevolnyi, *Nano Lett.* **2013**, *13*, 829.
- [30] Y. Kim, P. C. Wu, R. Sokhoyan, K. Mauser, R. Glauddell, G. Kafaie Shirmanesh, H. A. Atwater, *Nano Lett.* **2019**, *19*, 3961.
- [31] Y. Yifat, M. Eitan, Z. Iluz, Y. Hanein, A. Boag, J. Scheuer, *Nano Lett.* **2014**, *14*, 2485.
- [32] A. Pors, O. Albrektsen, I. P. Radko, S. I. Bozhevolnyi, *Sci. Rep.* **2013**, *3*, 2155.
- [33] A. Pors, M. G. Nielsen, S. I. Bozhevolnyi, *Optica* **2015**, *2*, 716.
- [34] G. Ding, K. Chen, X. Luo, J. Zhao, T. Jiang, Y. Feng, *Phys. Rev. Appl.* **2019**, *11*, 044043.
- [35] S. Tang, T. Cai, G. M. Wang, J. G. Liang, X. Li, J. Yu, *Sci. Rep.* **2018**, *8*, 6422.
- [36] H. Tan, J. Deng, R. Zhao, X. Wu, G. Li, L. Huang, J. Liu, X. Cai, *Laser Photonics Rev.* **2019**, *13*, 1800278.
- [37] J. Jung, T. Søndergaard, S. I. Bozhevolnyi, *Phys. Rev. B* **2009**, *79*, 035401.
- [38] N. Yu, P. Genevet, M. A. Kats, F. Aieta, J. P. Tetienne, F. Capasso, Z. Gaburro, *Science* **2011**, *334*, 333.
- [39] X. Zhang, Q. Li, F. Liu, M. Qiu, S. Sun, Q. He, L. Zhou, *Light: Sci. Appl.* **2020**, *9*, 76.